Journal of
Composites Science

MDPI

Article

Enhancing the Toughness of Composite Cold-Formed Steel Beams with ECC and Different Stiffener Arrangements and Shapes

Mahmoud T. Nawar [1,2,*], Ola A. Silem [3], Ishac Ibrahim [2], Hassan M. Maaly [2] and Yasser E. Ibrahim [1]

[1] Engineering Management Department, College of Engineering, Prince Sultan University, Riyadh 12435, Saudi Arabia; ymansour@psu.edu.sa
[2] Structural Engineering Department, Faculty of Engineering, Zagazig University, Zagazig 44519, Egypt; iishac@zu.edu.eg (I.I.); mtnawar@eng.zu.edu.eg (H.M.M.)
[3] Civil Engineering Department, High Institute for Engineering Technology-Al-Obour, 21K Cairo-Belbies Rd., Al-Obour 11828, Egypt; ola.abdallah@oi.edu.eg
* Correspondence: mnawar@psu.edu.sa

Abstract: This study investigates the toughness and load capacity of various innovative beam configurations of cold-formed steel beams (CFSB) using both ordinary concrete slabs and engineered cementitious composite (ECC) slabs. A finite element analysis with ABAQUS 20 was conducted on double-channel, sigma, G, and omega sections, both with and without inverted lips, as well as the effects of L, channel, and trapezoidal stiffeners and length-to-depth ratios. The double-omega section with ordinary concrete achieved the highest first peak load of 365.2 kN and a toughness increase of 181.1%. Inverted lips enhanced toughness in the double-G and sigma sections, with increases of 156.9% and 158.3%, respectively. Among ECC configurations, the double-omega section with ECC3 slab reached 387.4 kN and a toughness increase of 199.5%. Thinner ordinary concrete sections (70 mm and 90 mm) negatively impacted toughness, emphasizing the need for adequate thickness. Trapezoidal stiffeners also improved toughness. These findings highlight the importance of geometrical design and material selection in optimizing CFSB performance, offering valuable insights for future design practices.

Keywords: cold-formed steel; composite beam; engineered cementitious composites; omega section; sigma section; toughness

Academic Editor: Chensong Dong

Received: 17 November 2024
Revised: 20 December 2024
Accepted: 28 December 2024
Published: 7 January 2025

Citation: Nawar, M.T.; Silem, O.A.; Ibrahim, I.; Maaly, H.M.; Ibrahim, Y.E. Enhancing the Toughness of Composite Cold-Formed Steel Beams with ECC and Different Stiffener Arrangements and Shapes. *J. Compos. Sci.* **2025**, *9*, 24. https://doi.org/10.3390/jcs9010024

1. Introduction

Cold-formed steel sections play a significant role in promoting sustainable and eco-friendly construction. The light weight of cold-formed beams makes them more economical than hot-rolled ones [1]. Conversely, their thickness makes them susceptible to local, distortional, and lateral torsional buckling. Using the cold-formed section in composite structures with concrete combines the compressive strength of concrete and the tensile strength of steel through effective connectors between these two materials [2]. The first use of composite steel–concrete structures was in 1920 [3]. Composite cold-formed beams (CCFSBs) were studied in much research. Composite cold-formed steel C sections as floor joists under the effect of compressive load were studied to calculate the ultimate capacity [3,4]. Innovative shear connectors (BTTST) (bent-up triangular tab shear transfer) were studied in a push-out test [5]. The BTTST was also used in CFS–concrete composite beam specimens [6]. The ductility and strength capacity of a new innovative shear connector

for composite cold-formed beams were studied through push-out tests. These connectors were also applied to composite cold-formed steel beams [7,8]. Load-bearing capacity, deformation, flexural stiffness, and failure modes of a composite beam consisting of a lightweight concrete slab connected to a CFS built-up beam using bolted shear studs were obtained from experimental and numerical tests [9]. Experimental studies were conducted on composite cold-formed steel beams using lightweight concrete slabs and bolted shear connectors to examine the structural behavior of these innovative beams under both ambient and elevated temperatures [10]. Additionally, a numerical analysis was performed on these beams, considering various parameters such as section configurations, two grades of concrete, three slab thicknesses, and four heights of CFS sections, to inform the design of CFS–LWC composite beams [11]. Another experimental study focused on the construction of cold-formed steel lightweight concrete (CFS–LWC) composite beams with bolted shear connectors to evaluate their load-bearing capacity, deformation characteristics, and failure modes. This study also assessed the validity of the design predictions in accordance with EN 1994-1-1 for the CFS–LWC composite beams [12]. Innovative bolted shear connectors in demountable concrete were studied [13]. Numerical tests were conducted on a new type of demountable composite cold-formed steel beams using profiled steel sheets [14]. Finite element modeling was performed on a novel composite connection of bolted shear connectors embedded in grout. Single-t-composite cold-formed steel beams with concrete slabs were tested experimentally and numerically [15]. An experimental investigation of a composite beam with a new cold-formed U-shaped steel section and concrete was produced [16]. Numerical and analytical studies have explored the bending behavior of cold-formed steel–concrete composite beams [17]. A specific numerical investigation focused on bolted shear connections in these composite beams, examining various web configurations of the steel beam [18]. Additionally, a floor system comprising cold-formed steel, a corrugated steel deck, a concrete slab, and a furring channel as a novel shear connector was tested numerically to assess its structural behavior [19]. Both experimental and numerical studies have examined the structural performance of composite beams made from cold-formed steel (CFS) paired with a Ferro-cement slab [20]. Research involving push-out tests investigated the structural behavior of new shear connectors created by cutting rectangular sections from the top flange and web of the beam and bending them upward. The performance of composite cold-formed steel beams was evaluated experimentally and numerically using these innovative shear connector designs [21,22]. A comprehensive overview of advanced spot-welding techniques and innovative cold-formed steel–concrete composite solutions was also presented [23]. Furthermore, a numerical study was conducted on cold-formed steel lightweight concrete (CFS–LWC) composite beams with a corrugated web, focusing on two types of shear connectors: bolts and dowel rib connectors [24]. An experimental investigation was carried out on a composite floor system made up of thin-walled CFS trusses, a partially precast concrete slab, and innovative TWC shear connectors [25].

Using sigma cross sections for short beam-column increases the strength by 42% compared to the lipped channel sections [26]. The total load-carrying capacities of the lipped channel section to the sigma section for columns is 0.892 [27]. New omega, G, and sigma sections can improve the behavior of cold-formed steel beams against lateral torsional buckling [28]. The ultimate moment resistance of a continuous cold-formed sigma beam was calculated through a numerical study [29,30]. The moment capacity and failure modes of closed built-up beams made of two sigma sections were investigated numerically and experimentally [9,31]. The load capacity of the supported cold-formed sigma beam could be increased by adding glued steel tape [32]. Eight built-up cold-formed steel I-beams were tested experimentally to investigate the flexural capacity of such beams, which strengthened in the hollow web with different material [33].

While significant advancements have been made in the study of composite cold-formed beams (CCFSBs) under static loads, there remains a critical gap in understanding their full static resistance, particularly when utilizing innovative cold-formed steel (CFS) configurations in combination with engineered cementitious composite (ECC) slabs. Previous research has extensively explored various aspects of CCFSBs, including their load-bearing capacities and failure modes, but the integration of new CFS configurations and ECC materials has not been fully addressed.

This paper aims to bridge this gap by conducting a quasi-static numerical study of CCFSBs employing ECC slabs and new CFS configurations. Utilizing ABAQUS 20, an extensive parametric study was performed on various geometrical designs, including double channel, sigma, G, and omega sections, both with and without inverted lips. Additionally, the impact of L, channel, and trapezoidal stiffeners, along with length-to-depth ratios, was examined.

The novelty of this research lies in its focus on enhancing the full static responses of CCFSBs under severe loading conditions. By investigating the interplay between innovative configurations and materials, this study seeks to promote not only the strength and ductility of these beams but also their ability to sustain significant deformations without failure. The findings are expected to contribute valuable insights into the design and ap-plication of CCFSBs in sustainable construction, ultimately advancing the field of compo-site structural systems.

2. FE Modeling and Verification

2.1. Development of Numerical Verification Models

Finite element analysis (FEA) was conducted to create dependable models derived from experimental results [8], allowing for the simulation of the behavior of composite cold-formed beams. Three FE models were developed using ABAQUS/CAE [34]. ABAQUS/CAE software is the complete solution for finite element modeling for different structures under the effect of different loads. ABAQUS/CAE has tools so that you can create, edit, monitor, diagnose, and visualize simulations using advanced analyses.

2.2. Material Properties

The material of the cold-formed steel beams (CFSB) used in the finite element models of the proposed composite beams [8] has a yield strength of 518.4 MPa, an ultimate strength of 558.4 MPa, a Poisson's ratio of 0.3, and a Young's modulus of 187.4 GPa. A bilinear stress–strain model for (CFSB) was employed in the finite element study, as shown in Figure 1. The thickness of the steel beams is 2.3 mm.

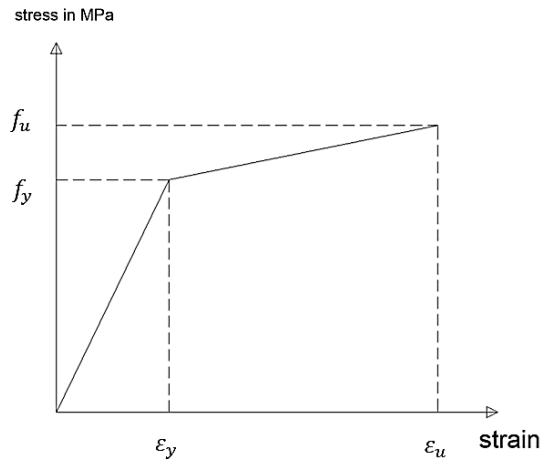

Figure 1. Bilinear stress–strain model of steel.

To accurately represent the behavior of the steel reinforcement within the slabs, a yield strength of 641 MPa, an ultimate strength of 676.9 MPa, and a Poisson's ratio of 0.3 were assigned. Furthermore, the elastic–plastic model with hardening was chosen to represent their behavior, in accordance with Eurocode 3, Eurocode 3, and [24,35–39].

To characterize the damage and failure mechanisms of concrete materials, the finite element model employed the concrete damage plasticity (CDP) model available in ABAQUS. This model incorporates two primary failure modes: tensile cracking and compressive crushing of concrete elements. Table 1 presents the parameters for the concrete damage plasticity model. The cylindrical compressive strength of the concrete is 23 MPa, with a Young's modulus (Ec) of 20,600 MPa and a Poisson's ratio (υ) of 0.15 [8].

Table 1. The concrete plasticity properties.

Dilation Angle (Ψ)	Eccentricity (ε)	(σb0/σc0)	k	Parameter Viscosity μ
56	0.05	1.16	0.667	0

To effectively represent the non-linear stress–strain behavior of ordinary concrete, established material models were utilized [40,41], as shown in Equations (1)–(5).

$$\sigma_c = f_c \left[\frac{\beta\left(\frac{\varepsilon_c}{\varepsilon_{c0}}\right)}{\beta - 1 + \left(\frac{\varepsilon_c}{\varepsilon_{c0}}\right)^{\beta}} \right] \tag{1}$$

$$\sigma_t = \begin{cases} f_t \left[1.2 * \left(\frac{\varepsilon_t}{\varepsilon_{t0}}\right) - 0.2\left(\frac{\varepsilon_t}{\varepsilon_{t0}}\right)^6 \right] & 0 \le \varepsilon_t \le \varepsilon_{t0} \\ f_t \left[\frac{\frac{\varepsilon_c}{\varepsilon_0}}{1.25\left(\frac{\varepsilon_t}{\varepsilon_{t0}} - 1\right)^2 - \frac{\varepsilon_t}{\varepsilon_{t0}}} \right] & \varepsilon_{t0} \le \varepsilon_t \end{cases} \tag{2}$$

$$\beta = \frac{f_c}{32.4} + 1.55 \tag{3}$$

where σ_c and ε_c are the concrete stress and strain, respectively, and f_c and ε_{c0} are the ultimate stress and strain in compression.

Damage parameters for concrete [35,42] can be determined by the following:

$$d_c = 1 - \frac{\sigma_c}{f_c} \tag{4}$$

$$d_t = 1 - \frac{\sigma_t}{f_t} \tag{5}$$

where d_c is the damage parameter in compression and d_t is the damage parameter in tension.

2.3. Geometry, Loading, and Boundary Condition

Full-scale beams [8] were modeled in ABAQUS software. The steel beam consists of two back-to-back lipped C-channels with a depth of 250 mm, and a concrete slab perpendicular to the steel beam axis was formed by applying a profile metal deck. To build a durable composite beam, see Figure 2. Three different kinds of shear connectors (SBSC, DBSC, and HPSC), as in Figure 2c, were placed between the slab and the beam. The shear connectors length 100 mm, width 78 mm, and depth 190 mm. Each beam was 4360 mm long and the span was 4000 mm. The concrete slabs were 1000 mm wide and 110 mm.

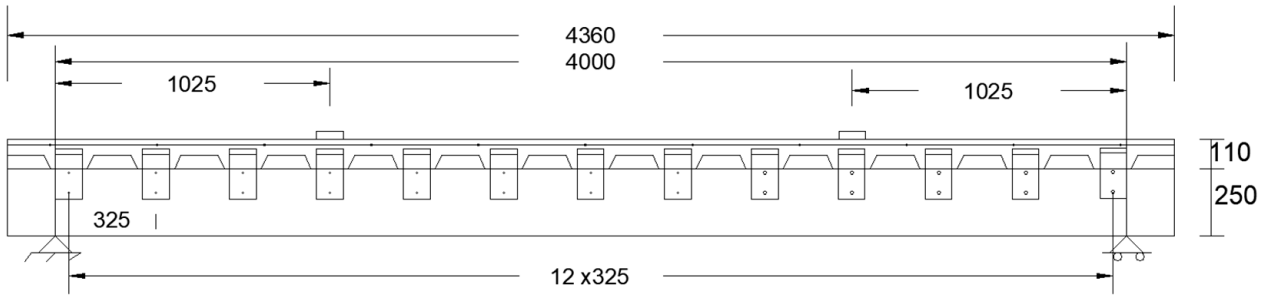

(**a**) Shear connectors arrangements

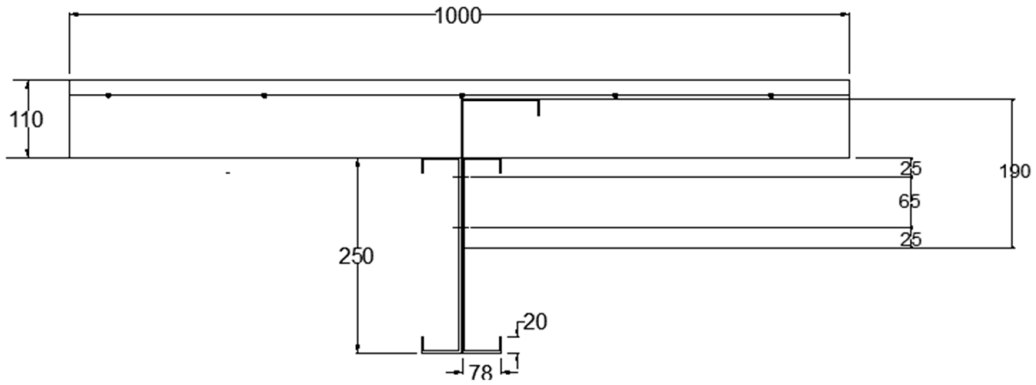

(**b**) Cross section

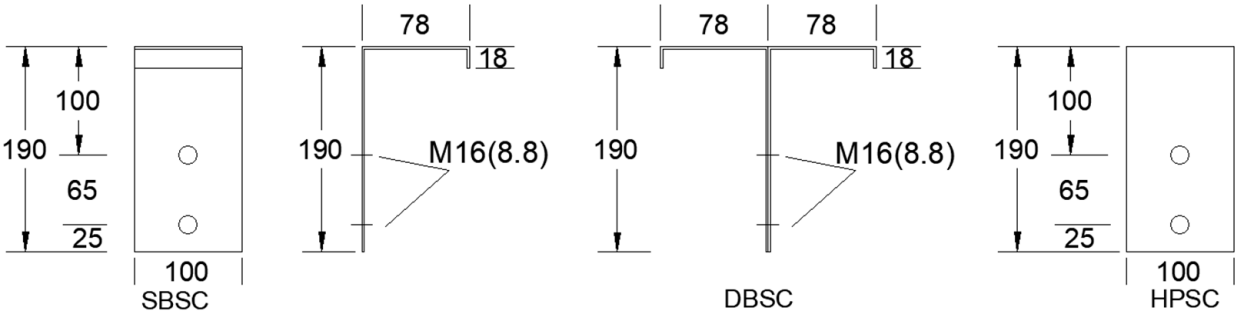

(**c**) Types of shear connectors

Figure 2. Configuration of the verified numerical models and the shear connectors used, dimensions in mm.

The three verified models are composite beam with single angle (SBSC) as shear connectors (FSSBSC250-23), composite beam with plate as shear connectors (FSHPSC250-23) and non-composite beam (FSSC250-23). All beams had a 2.3 mm thickness, but the shear connector thickness was 1.5 mm for all types [8].

The beam and shear connectors are modeled with shell elements, while the concrete slab, which has a thickness of 110 mm and a width of 1000 mm, is modeled using solid elements. The reinforcing bars, with a diameter of 6 mm, are represented by truss elements. Loads were applied to the top of the concrete slab using the coupling option available in ABAQUS/CAE. Displacement control was employed to simulate a four-point loading system for the simply supported beams, with one end of the beam fixed as a hinge and the other end supported by a roller.

2.4. FE Meshing, Interaction, and Analysis Method

A sensitivity study was conducted to evaluate mesh element sizes of 50 mm, 20 mm, 10 mm, and 5 mm for steel, and 100 mm, 50 mm, and 20 mm for concrete, until no significant changes in the results were observed. Figure 3 illustrates the peak load for the different mesh sizes. Ultimately, a mesh size of 50 mm for concrete and 10 mm for steel was selected. A two-node linear 3D truss was used to model the reinforcing bars. Truss elements were employed for representing the reinforcement bars [40,43–47]. The steel beam and shear connectors were modeled using a four-node doubly curved shell element with reduced integration, hourglass control, and finite membrane strains (S4R). For the concrete slab, an eight-node linear brick element with reduced integration and hourglass control (C3D8R) was used.

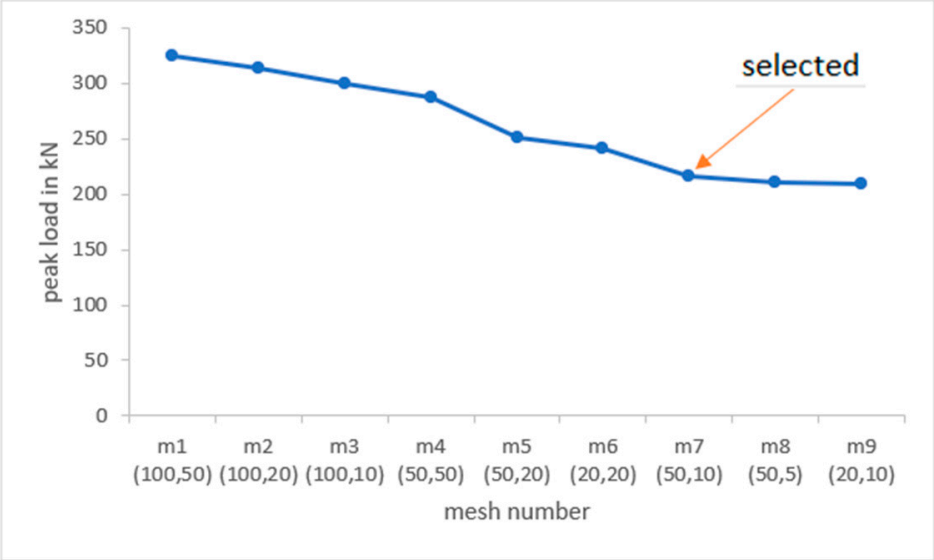

Figure 3. Convergence study for the composite cold-formed beam (FSSBSC250-23).

Surface-to-surface contact was implemented between the concrete slab and the steel beam to simulate the interaction between the adjoining components. Embedded constraints were applied for the reinforcing bars, shear connectors, and concrete slabs. The angle shear connectors and the two channels were bolted together using two M16 (8.8) bolts at each shear connector during the experimental test. To simulate these connections, surface-to-surface contact was first established between the web of each channel and the adjoining surface of the angle shear connector. Then, the fastener tool available in ABAQUS was employed to model the bolts connecting the two channels and the angle shear connectors. The implicit solver in ABAQUS was employed to analyze the finite element models as a quasi-static analysis. Figure 4 illustrates the assembled model after meshing.

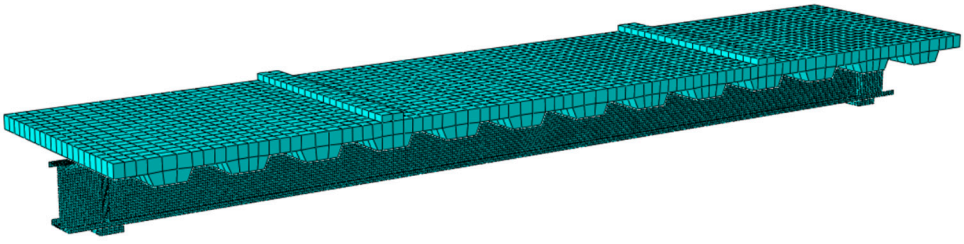

Figure 4. Meshing of the assembled model in ABAQUS.

2.5. Results of Verified Models

Three finite element (FE) models were developed and validated against the experimental results presented by S. O. Bamaga et al. [8]. Two of these models represent composite cold-formed steel (CFS) beams with a concrete slab and shear connectors, referred to as FSSBSC250-23 and FSHPSC250-23. The third model is a non-composite CFS beam, designated FSSC250-23.

Load-deflection curves for both the numerical and experimental results of the three specimens are listed in Table 2 and plotted in Figure 5. The failure mode for the composite beams involved web failure beneath the point loads and cracks in the concrete slab, as shown in Figures 6 and 7. To visualize cracks, a mesh size of 20 was used. Reducing the mesh size of the concrete only did not result in any changes to the peak load and deflection results. Figure 8 illustrates the failure mode of the non-composite beam. Overall, there was a good correlation between the FE and experimental results.

Table 2. Comparison of the experimental and finite element findings.

Modal Annotation	Peak Load (kN)			Deflection at Peak (mm)			Maximum Deflection (mm)		
	EXP.	FE	Diff. %	EXP.	FE	Diff. %	EXP.	FE	Diff. %
FSSBSC250-23	187.7	215.8	14.9	34.2	30.7	−10.2	37.1	50.4	35.8
FSHPSC250-23	194.07	225.1	15.9	38.4	34.6	−9.8	40.2	40.5	0.74
FSSC250-23	71	75.2	5.9	20	20.5	2.5	20	20.5	2.5

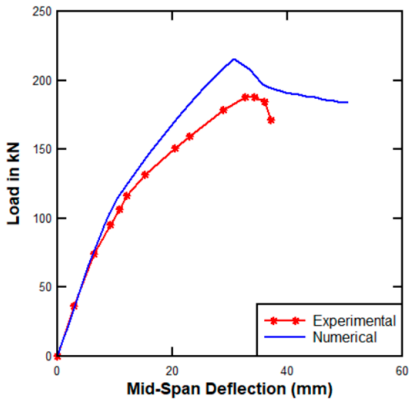

(**a**) FSSBSC250-23

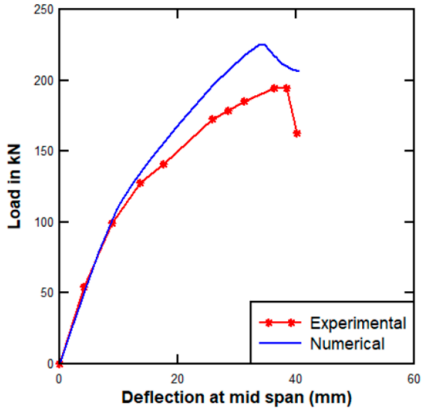

(**b**) FSHPSC250-23

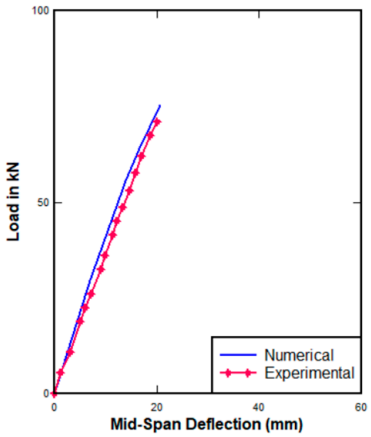

(**c**) FSSC250-23

Figure 5. Load-deflection curves for verified beams.

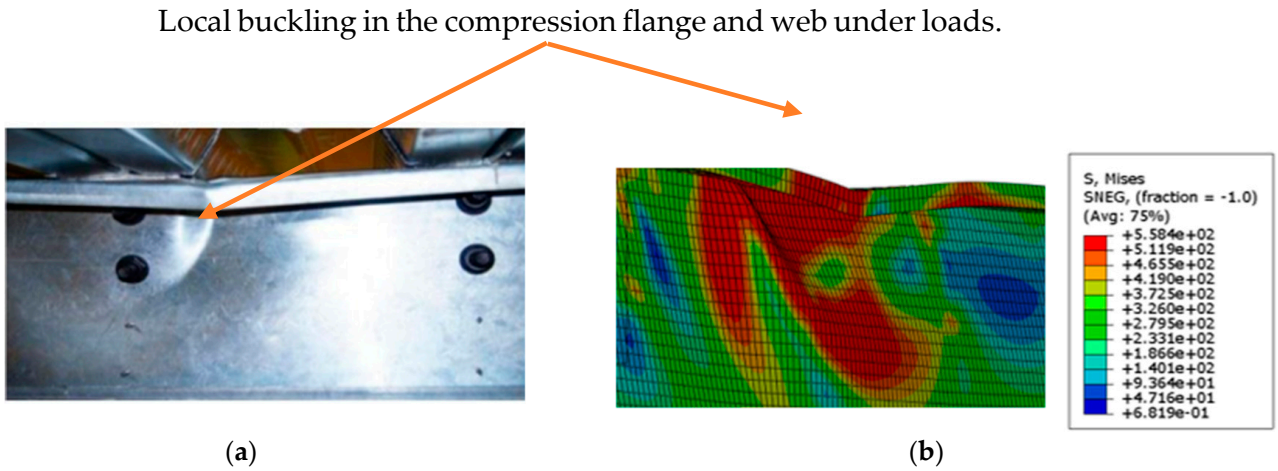

Figure 6. Experimental (FSSBSC250-23 and FSHPSC250-23) and numerical model (failure modes of CFSB). (**a**) Experimental [8]. (**b**) Numerical model.

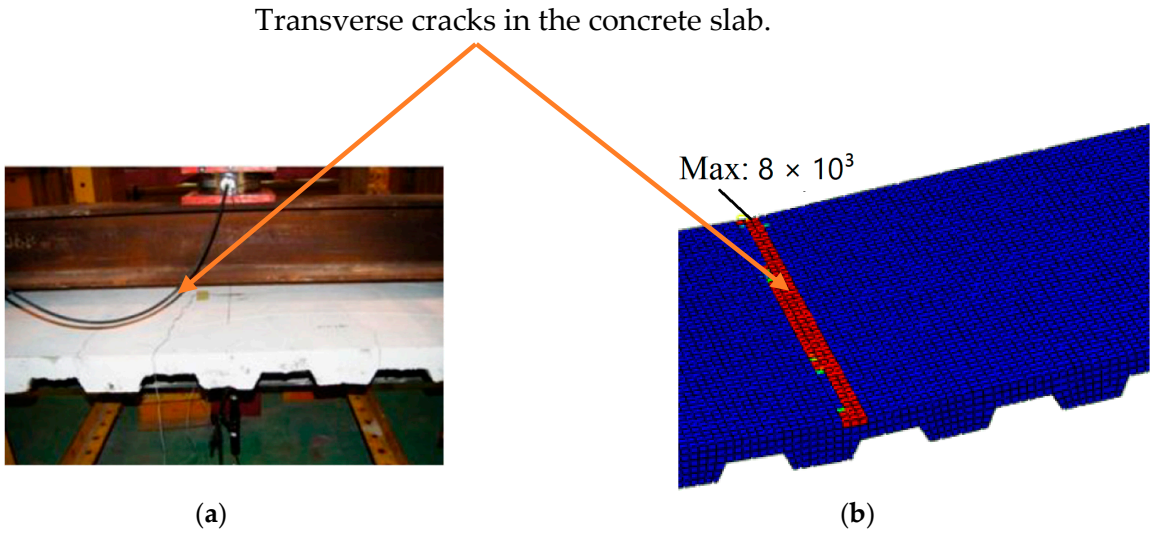

Figure 7. Experimental and numerical model (failure mode of the concrete slab). (**a**) Experimental [8]. (**b**) Numerical model.

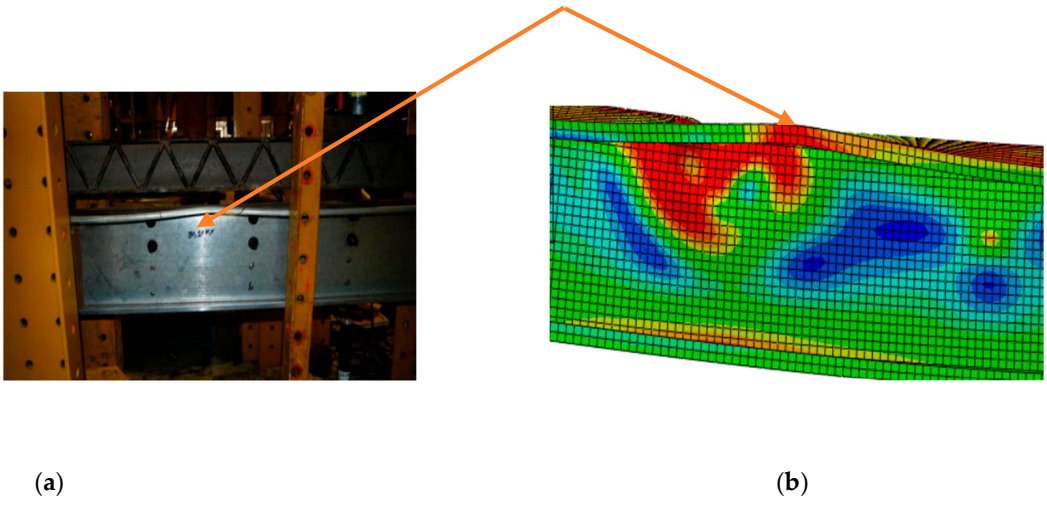

Figure 8. Experimental (FSSC250-23) and numerical model (failure mode of the non-composite beam). (**a**) Experimental, [8]. (**b**) Numerical model.

The FE model generally predicts higher load capacities than the experimental results across all test cases. The differences range was from 5.9% to 15.9%. The FE model predicts lower deflections than the experimental results for the first two test cases (FSSBSC250-23 and FSHPSC250-23), indicating that the model may be underestimating the deflection behavior of the structures under peak load.

In contrast, for the FSSC250-23 test case, the FE model predicts a slightly higher deflection (20.5 mm) compared to the experimental result (20 mm), suggesting better alignment in this specific scenario.

3. Parametric Study

Three main stages define the entire static resistance: the bending zone, the softening phase, and the tension-membrane phase, as illustrated in Figure 9. Within this behavior, two critical limit points are identified: the snap-through point and the failure point. An extensive parametric study was conducted to explore the factors that influence the overall static resistance of composite cold-formed steel beams (CCFSBs), shown in Figure 2. This study considered several parameters, including the effects of using new sections (sigma, omega, G, G with inverted lips, and sigma with inverted lips), Figure 10, for the CCFSB, incorporating engineered cementitious composite (ECC), and stiffening the CCFSB with different cross sections at various spacings. Additionally, it examined the thickness of the stiffeners and shear connectors, and the thickness of the concrete slab. These parameters were categorized as the first group of the parametric study. The second group focused on varying the length-to-depth ratio of the CFSB. Thus, the cases studied can be divided into two groups: group one and group two.

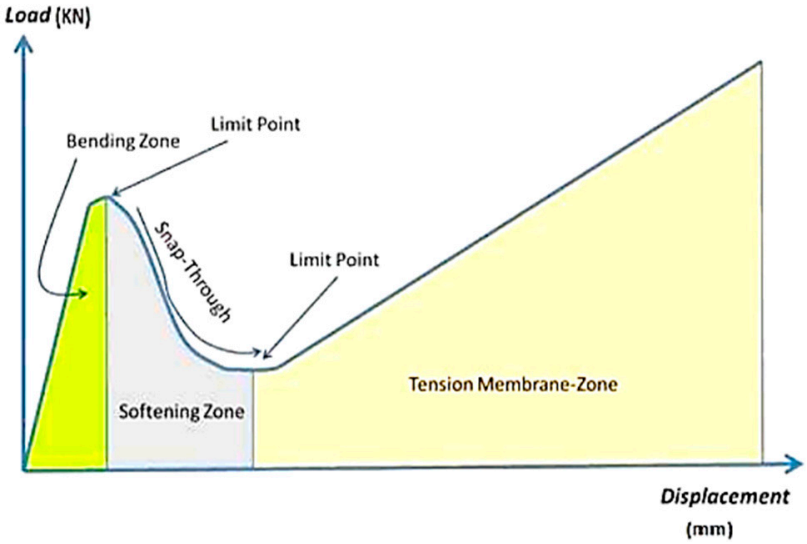

Figure 9. General profile for static resistance response of CCFSBs.

3.1. Group One

In the first group of the parametric study, various parameters were considered, as previously mentioned. To facilitate clear identification and organization of each model, a specific notation system was implemented. Each model is assigned a unique identifier in the format (A-B-C-D-E) as in Table 3 where

"A "represents the type of cross section of the steel beam.

- DC series (double channels BTB);
- DS series (double sigma BTB);
- DO series (double omega BTB);
- DG series (double G BTB);

- DGi series (double G BTB with inverted lips);
- DSi series (double sigma BTB with inverted lips).

"B" indicates the incorporation of the type of the used concrete.

- OC is ordinary concrete followed by its thickness;
- ECC1, 2 and 3 are engineering cementitious composites.

"C" refers to the thickness of the concrete slab.

- Thicknesses of 70, 90, 110, 130, 150, and 200 mm were studied.

"D" refers to the type of stiffener followed by its number along the web.

- L6 and L11 are L-shaped stiffeners at 650 mm and 325 mm spacing, respectively;
- Tr6 and Tr11 are trapezoidal-shaped stiffeners at 650 mm and 325 mm spacing, respectively;
- C6 and C11 are channel-shaped stiffeners at 650 mm and 325 mm spacing, respectively;
- SH11 is an extended shear connector as a stiffener at 325 mm spacing.

"E" specifies the thickness of the used stiffener in mm.

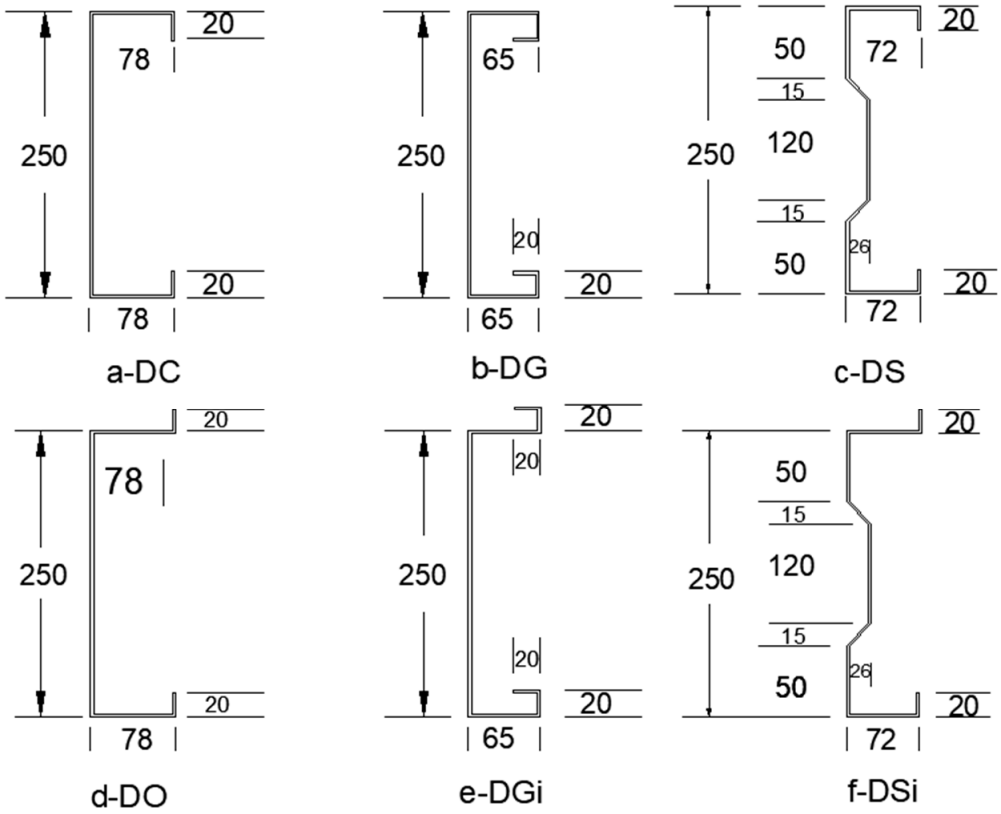

Figure 10. Dimensions of different CFSB cross sections in mm.

Table 3. The parameters of the first group of parametric study.

No.	Model Notation	No.	Model Notation
1	DS-OC-110	17	DC-OC-130
2	DO-OC-110	18	DC-OC-150
3	DG-OC-110	19	DC-OC-200
4	DGi-OC-110	20	DC-OC-110-L6-2.3
5	DSi-OC-110	21	DC-OC-110-L11-2.3
6	DC-OC-110	22	DC-OC-110-C6-2.3

Table 3. *Cont.*

No.	Model Notation	No.	Model Notation
7	DC-ECC1-110	23	DC-OC-110-C11-2.3
8	DC-ECC2-110	24	DC-OC-110-TR6-2.3
9	DC-ECC3-110	25	DC-OC-110-TR11-2.3
10	DS-ECC3-110	26	DC-OC-110-TR11-1
11	DG-ECC3-110	27	DC-OC-110-TR11-2
12	DO-ECC3-110	27	DC-OC-110-TR11-3
13	DGi-ECC3-110	29	DC-OC-110-SH11-1.5
14	DSi-ECC3-110	30	DC-OC-110-SH11-1
15	DC-OC-70	31	DC-OC-110-SH11-2
16	DC-OC-90	32	DC-OC-110-SH11-3

3.1.1. Section Geometry

Channel, sigma, omega, G, G with inverted lips, and sigma with inverted lips cross sections were used, each having the same volume, depth, area, and length of lip, as shown in Figure 10. The dimensions and configurations of these sections are detailed in Figure 10. Channel, omega, sigma, inverted sigma, G, and inverted G sections weigh 7.88, 7.88, 7.97, 7.97, 8.05, and 8.05 kg/m. All sections have almost the same volume per meter. The dimensions of the sigma section were based on the work of L. Laím et al. and R. Rahnavard et al. [26,48]. Embedded constraint available in ABAQUS was implemented to simulate the interaction between the inverted lips and the concrete slab. To select the embedded accurate parts in the concrete slab, the inverted lips were partitioned matching the concrete slab geometry.

3.1.2. Concrete Type and Thickness

Four types of concrete were used in the models: ordinary concrete for the main reference model and engineered cementitious composite (ECC) for three additional models. The properties of ECC were obtained from the work of X. Nie et al. [49–54]. Table 4 presents the maximum tensile and compressive strengths of the ECC used. Six different cold-formed steel (CFS) cross sections were applied to the ECC3 slab. Additionally, six thicknesses—70 mm, 90 mm, 110 mm, 130 mm, 150 mm, and 200 mm—were studied for the concrete slab. The stress–strain relationship of ECC in compression and tension was developed by Equations (6) and (7) [55].

$$\sigma_c = \begin{cases} E_0\,\varepsilon_c & \varepsilon_c \le 0.4\varepsilon_{cp} \\ E_0\,\varepsilon_c\left(1 - 0.308\frac{E_0\varepsilon_c}{f_c} + 0.124\right) & 0.4\varepsilon_{cp} < \varepsilon_c \le \varepsilon_{cp} \end{cases} \quad (6)$$

$$\sigma_t = \begin{cases} \frac{\sigma_{tc}}{\varepsilon_{tc}}\ \varepsilon_t & 0 \le \varepsilon_t \le \varepsilon_{tc} \\ \sigma_{tc} + \frac{\sigma_{tu}-\sigma_{tc}}{\varepsilon_{tu}-\varepsilon_{tc}}\left(\varepsilon_t - \varepsilon_{tc}\right) & \varepsilon_{tc} < \varepsilon_t \end{cases} \quad (7)$$

where ε_{cp} represents the compressive strain at the peak stress f_c, E_0 is the elastic modulus, σ_{tc} and ε_{tc} are the stress and strain, in tension, at crack initiation, and σ_{tu} and ε_{tu} are the ultimate tensile stress and its corresponding strain, respectively.

Table 4. ECC properties, stresses in MPa.

	Maximum Compressive Strength	Maximum Tensile Strength
ECC1	28	4
ECC2	28	8
ECC3	55.8	4.2

3.1.3. Type and Configurations of Proposed Stiffeners

To enhance the strength of the double channel composite cold-formed steel beam (CCFSB), three types of stiffeners were employed: L section, C section, and trapezoidal section, as illustrated in Figure 11a,b. The stiffeners were designed with a depth equal to that of the web of the CFSB, a uniform thickness of 2.3 mm for all types, and a width of 100 mm for both the L and C sections. The dimensions of the trapezoidal section were derived from the research of M. Divya et al. [56]. In ABAQUS, the stiffeners were modeled using four-node doubly curved shell elements with reduced integration, hourglass control, and finite membrane strains (S4R), matching the beam's mesh size of 10 mm. These stiffeners were connected to the webs of each channel of the beam using fasteners, as illustrated in Figure 11c. Each type of stiffener was arranged at two different spacings: 325 mm and 650 mm along the web. Additionally, to investigate the effect of thickness, three variations—1 mm, 2 mm, and 3 mm—were examined for the trapezoidal section.

3.1.4. Shear Connectors

1.5 mm L-shaped shear connectors were installed between the two back-to-back CFS channels to ensure full interaction between the concrete slab and the steel beams, as shown in Figure 12. To evaluate their effectiveness in stiffening the steel beam, the thickness of the shear connectors was varied. Three thicknesses—1 mm, 2 mm, and 3 mm—were modeled, and the results were compared to those of the main model, which utilized a thickness of 1.5 mm.

3.2. Group Two

In the second group of the parametric study, three spans (3000 mm, 4000 mm, and 6000 mm) with varying depths were analyzed to evaluate the effect of the span-to-depth ratio for the CCFSB with a back-to-back double-channel section with a thickness of 2.3 mm. The span and depth of the steel beams were determined in accordance with the North American specifications for the design of cold-formed steel members [57]. Each model is designated with a notation (A-B-C), as detailed in Table 5.

Table 5. Parameters of the second group.

NO	Group Two			
	Model Notation	CFSB		
		Span-to-Depth Ratio (L/D)	Length mm	Depth mm
1	DC-3-8	8	3000	375
2	DC-4-8		4000	500
3	DC-6-8		6000	750
4	DC-3-10	10	3000	300
5	DC-4-10		4000	400
6	DC-6-10		6000	600

Table 5. *Cont.*

NO	Group Two			
	Model Notation	CFSB		
		Span-to-Depth Ratio (L/D)	Length mm	Depth mm
7	DC-3-16	16	3000	187.5
8	DC-4-16		4000	250
9	DC-6-16		6000	375
10	DC-3-20	20	3000	150
11	DC-4-20		4000	200
12	DC-6-20		6000	300

Where "A" refers to the type of cross section of the steel beam DC series (double channels BTB). "B" refers to the length of the steel beam in m. "C" refers to the length-to-depth ratio of the CFSB.

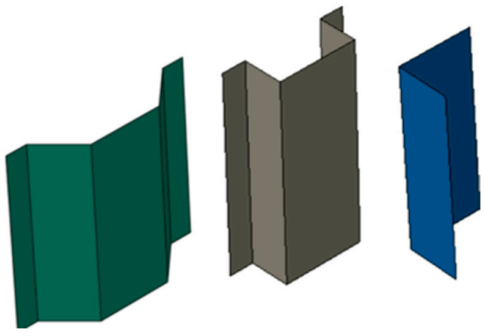

(**a**) 3D FE of trapezoidal, C-section, and L-section stiffeners.

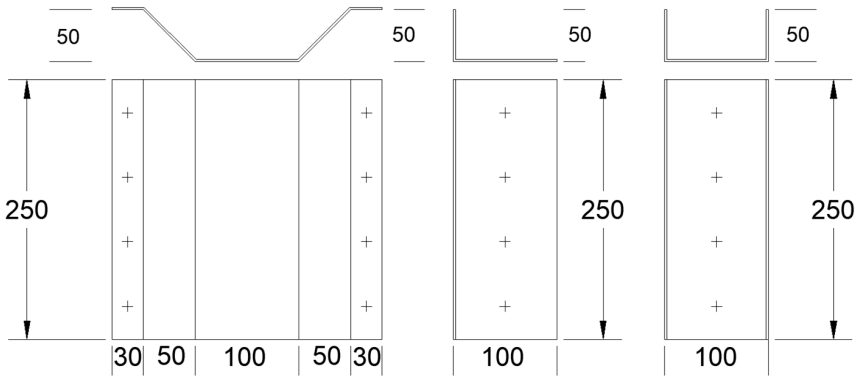

i-TR ii-L ii-C

(**b**) Dimensions of trapezoidal, L-section, and C-section stiffeners in mm

i-L ii-TR

(**c**) Arrangement of fasteners in ABAQUS

Figure 11. Types and configurations of proposed stiffeners.

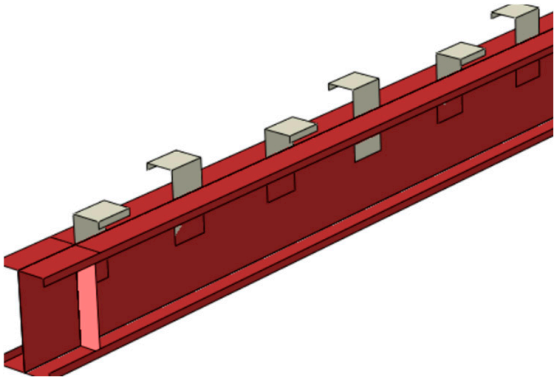

(**a**) Finite element configuration of the shear connectors

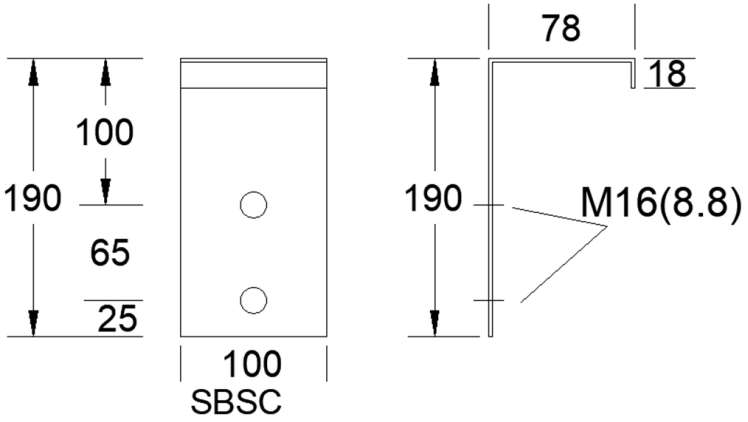

(**b**) Dimensions of the shear connectors in mm.

Figure 12. Lipped angles as shear connectors between the two channels, 1.5 mm thickness.

4. FE Results and Discussion

4.1. Failure Criteria

The failure criteria for composite cold-formed steel beams (CCFSBs) vary based on the stiffening strategies employed. In the first group of specimens, the predominant failure mode was local buckling in the compression flange and at the compression portion of the webs, as illustrated in Figure 13. In contrast, the failure modes for sections with inverted lips (omega, G, and sigma) differed from those without inverted lips. For these sections, failure was characterized by yielding in the tension flange and some distortion in the web, as shown in Figure 14. Embedding the lips within the concrete slab effectively reduces or prevents local buckling in the flanges; however, it may exacerbate cracking in the concrete slab. Notably, the use of engineered cementitious composite (ECC) mitigates slab cracking in models with inverted lips, demonstrating its beneficial impact on overall performance.

Concrete thicknesses of 70 mm, 90 mm, 110 mm, 130 mm, 150 mm, and 200 mm were investigated. As the thickness of the concrete increased, the failure modes transitioned from local buckling in the compression flange for thicknesses of 70 mm, 90 mm, 110 mm, and 130 mm, see Figure 15a, to distortion in the same flange for thicknesses of 150 mm and 200 mm, see Figure 15b. Using stiffeners causes more distortion in the compression flanges under loads, as in Figure 16.

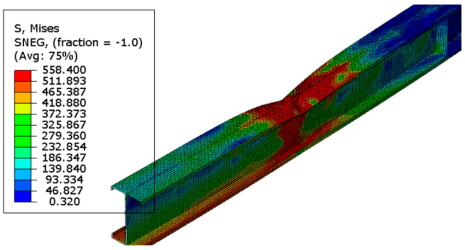

(**a**) DC-OC-110

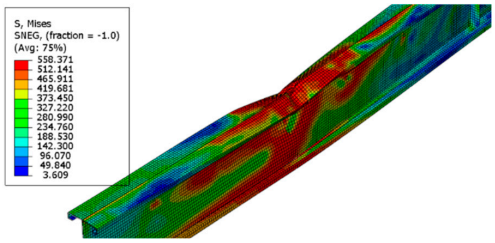

(**b**) DG-OC-110

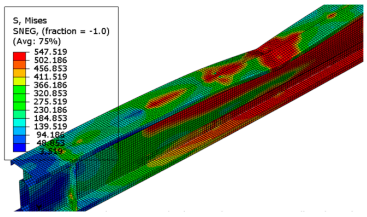

(**c**) DS-OC-110

Figure 13. Failure modes for DC-OC-110, DG-OC-110, and DS-OC-110 (local buckling in the compression flange and at the compression portion of the web).

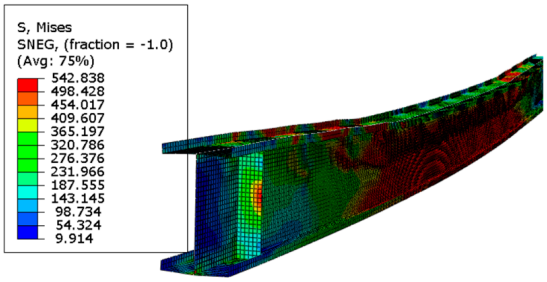

(**a**) DO-OC-110

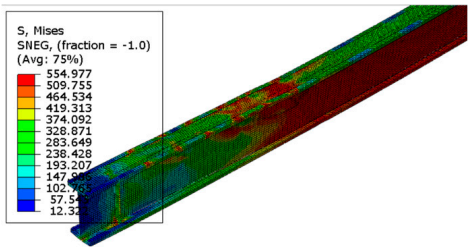

(**b**) DGi-OC-110

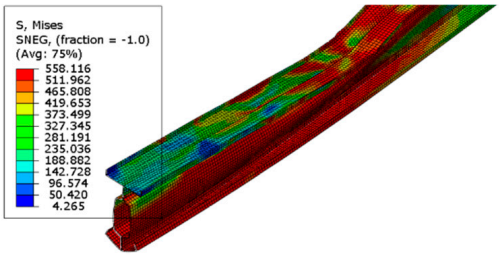

(**c**) DSi-OC-110

Figure 14. Failure modes for different section geometry with inverted lips (yielding in the tension flange and some distortion in the web).

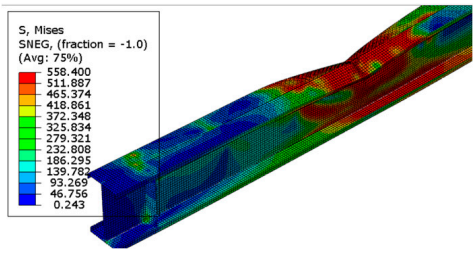

(**a**)

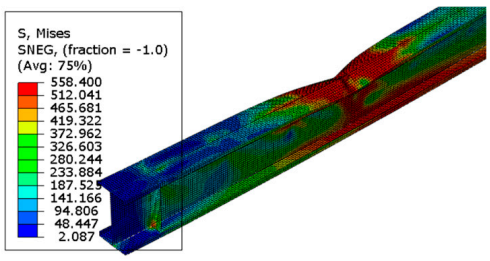

(**b**)

Figure 15. Failure modes for the concrete slabs with thicknesses of 70, 90, 110, 130 mm, 150 mm, and 200 mm. (**a**) Local buckling in the compression flange for thicknesses of 70, 90,110 and 130 mm; (**b**) distortion in the compression flange for thicknesses of 150 and 200 mm.

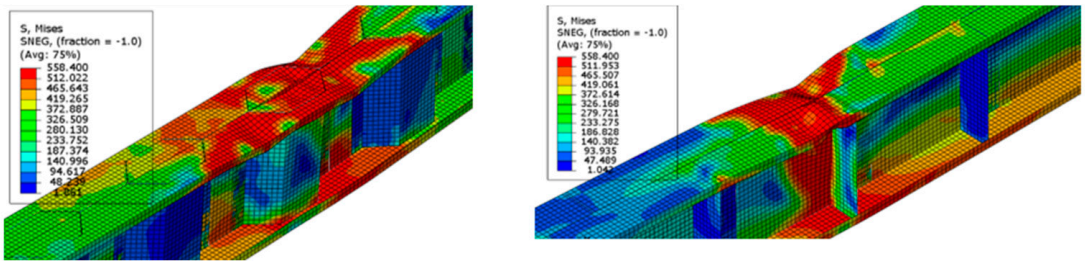

(**a**) DC-OC-110-TR11-2.3 (**b**) DC-OC-110-L11-2.3

Figure 16. Failure modes for DC-OC-110-TR11-2.3and DC-OC-110-L11-2.3 (distortion in the compression flanges under loads).

In the second group, the failure criteria for specimens with a span-to-depth ratio of 20 or 16 were characterized by local buckling in the compression flange and web, as shown in Figures 17 and 18. In contrast, models with a span-to-depth ratio of 10 or 8 exhibited failure modes of distortional buckling in the flanges or shear buckling in the web, as illustrated in Figures 19 and 20.

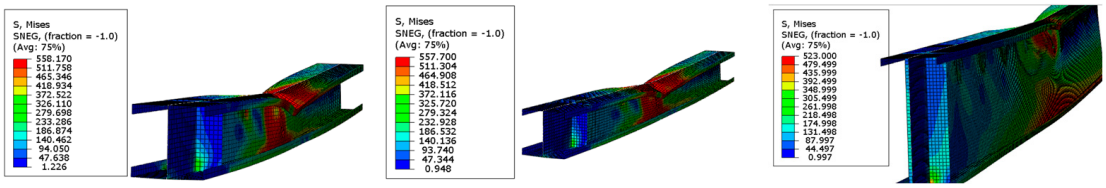

(**a**) span 3 m (**b**) span 4 m (**c**) span 6 m

Figure 17. Failure modes for models with span-to-depth ratio of 20 (local buckling in the compression flange and web).

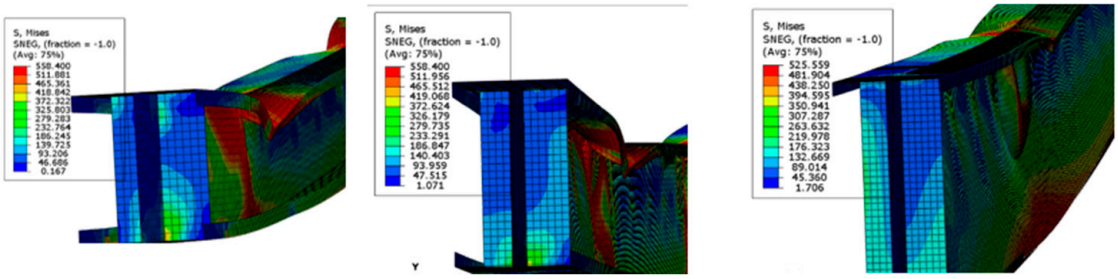

(**a**) span 3 m (**b**) span 4 m (**c**) span 6 m

Figure 18. Failure modes for models with span-to-depth ratio of 16 (local buckling in the compression flange and web).

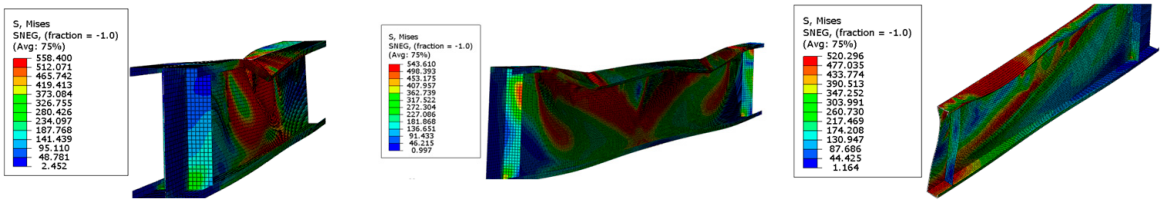

(**a**) span 3 m (**b**) span 4 m (**c**) span 6 m

Figure 19. Failure modes for models with span-to-depth ratio of 10 (distortional buckling in the flanges or shear buckling in the web).

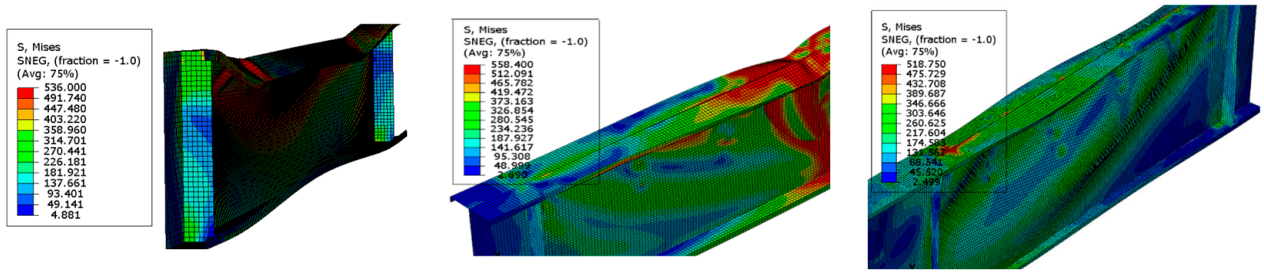

(**a**) span 3 m (**b**) span 4 m (**c**) span 6 m

Figure 20. Failure modes for models with span-to-depth ratio of 8 (distortional buckling in the flanges or shear buckling in the web).

4.2. Load Deflection Relationship

To investigate the effects of various parameters on the peak load and the corresponding deflection at this peak load, load-deflection curves were plotted for all models analyzed using the finite element (FE) method, as shown in Figures 21–25.

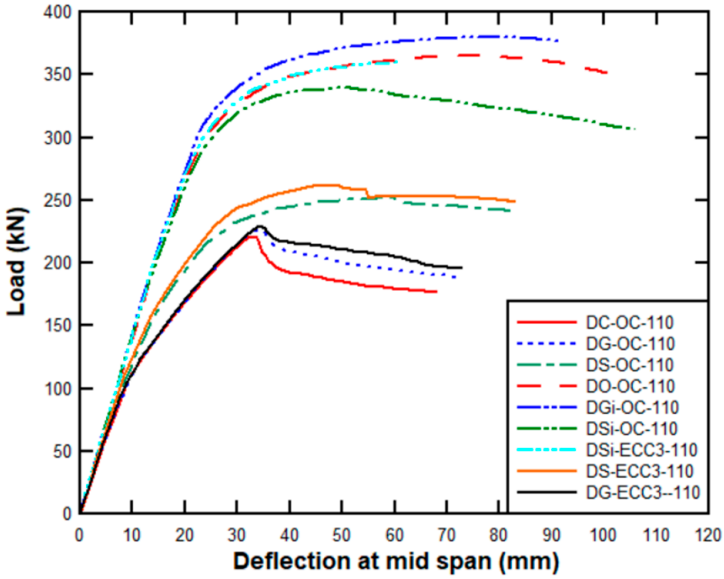

Figure 21. Load-deflection curves showing the effect of using the different CFS cross sections (sigma, omega, G, Gi, and Si).

4.2.1. Effect of Different CFS Configurations with Ordinary Concrete and ECC Slabs (110 mm)

The analysis of these results highlights the performance differences between different beams with the various beam configurations with ordinary concrete slabs and ECC slabs, as seen in Figures 21 and 22.

The double-G section with an inverted lip and ECC3 slab exhibited the highest peak load of 400.7 kN, closely followed by the double-omega section with ECC3 slab at 387.4 kN. These results suggest that incorporating inverted lips and utilizing ECC3 significantly enhances load-carrying capacity.

The double-sigma section with inverted lips and ECC3 slab also performed well, reaching 384 kN. In contrast, the configurations with ordinary concrete slabs, such as the double-channel section (221.3 kN) and the double-sigma section (251.5 kN), demonstrate significantly lower peak loads, highlighting the advantages of ECC.

The deflection at peak load varied across the specimens, with the double-G section with inverted lips and ECC3 slab showing the highest deflection of 77.8 mm. This indicates

that while this configuration can handle substantial loads, it also experiences significant deflection under loading and consequently significant resilience.

In contrast, sections with ordinary concrete, like the double-channel and double-G sections, exhibited lower deflections at peak loads (e.g., 33.3 mm and 33.6 mm, respectively).

In summary, the introduction of ECC slabs generally resulted in improved load-carrying capacities across various beam configurations. Also, the presence of inverted lips in sections like the double G and double sigma significantly contributed to their load-carrying capacity.

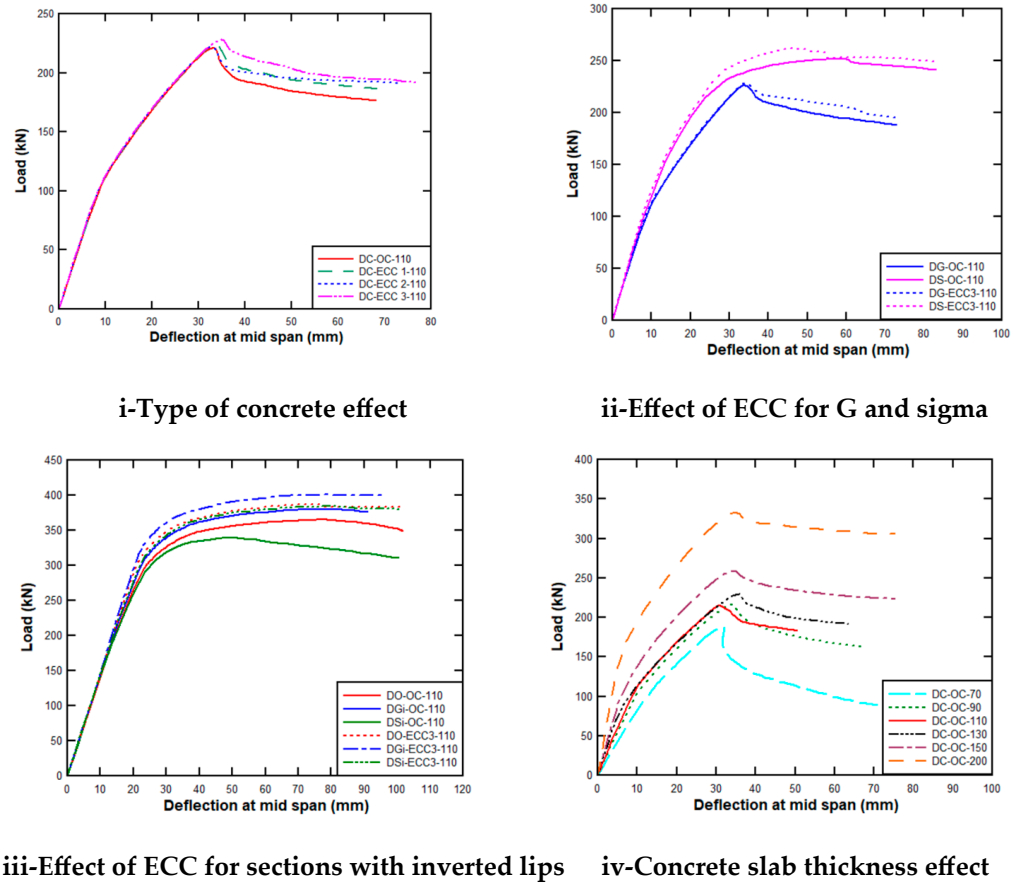

i-Type of concrete effect **ii-Effect of ECC for G and sigma**

iii-Effect of ECC for sections with inverted lips **iv-Concrete slab thickness effect**

Figure 22. Load-deflection curves showing the effect of using the different concrete types and thicknesses.

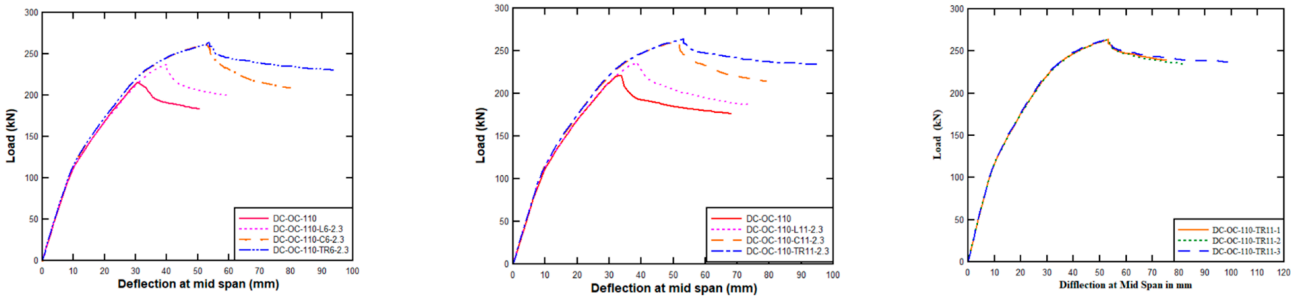

(i) **(ii)** **(iii)**

Figure 23. Load-deflection curves showing the effect of using the different types of stiffeners at different spacings. (**i**) Stiffeners were arranged at a spacing of 650 mm; their numbers are 6 along the web. (**ii**) Stiffeners were arranged at a spacing of 325 mm, their numbers are 11. (**iii**) Effect of the stiffeners' thickness.

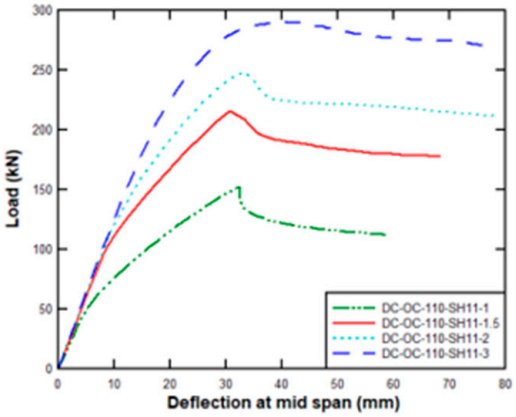

Figure 24. Load-deflection curves showing the effect of shear connectors' thickness.

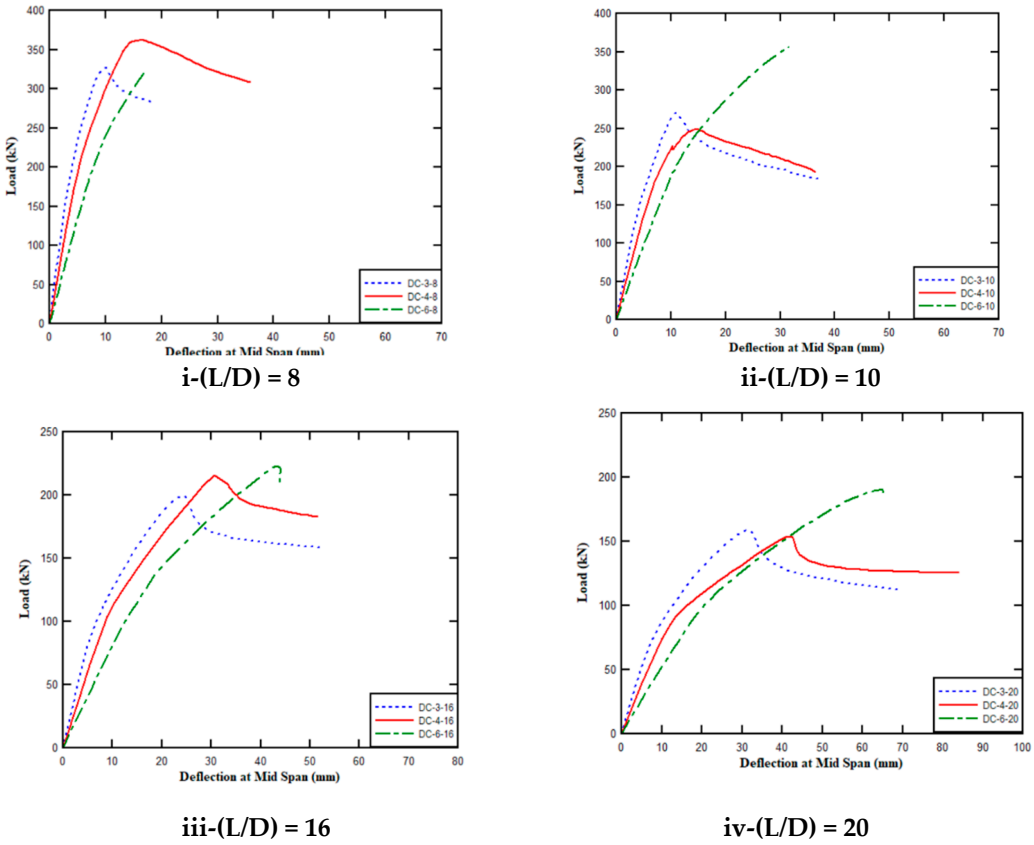

Figure 25. Load-deflection curves for the second group.

4.2.2. Effect of the Thickness of Ordinary Concrete Slabs

Six thicknesses—70 mm, 90 mm, 110 mm, 130 mm, 150 mm, and 200 mm—were studied to find the maximum load and deflection for the double-channel composite cold-formed steel beam with OC slabs, see Figure 22. The first peak load increases with the increase in the concrete slab thickness. The lowest load capacity is observed in the 70 mm thickness model at 187.6 kN, while the highest peak load of 332.5 kN is achieved with the 200 mm thickness. This trend indicates a direct correlation between slab thickness and load capacity, suggesting that thicker concrete slabs provide greater resistance to applied loads.

4.2.3. Effect of the Configurations of Proposed Stiffeners

The provided results detail the performance of double-channel sections with ordinary concrete (OC) slabs, focusing on various stiffener configurations (L, channel, and trapezoidal) and their influence on structural performance, see Figure 23.

The introduction of stiffeners generally increases the first peak load across all configurations. The highest first peak load is observed in the double-channel section with the trapezoidal stiffener at 325 mm, reaching 263.5 kN. Both types of channel stiffeners exhibit a notable increase in peak load compared to the L stiffeners, with the channel stiffener at 325 mm showing a peak load of 262.6 kN, indicating that the geometry of the stiffener can significantly enhance load capacity.

4.2.4. Effect of the Thickness of Shear Connectors

Four thicknesses—1 mm, 1.5 mm, 2 mm, and 3 mm—were studied to find the maximum load and deflection for the double-channel composite cold-formed steel beam with OC slabs, see Figure 24. The first peak load increases with the increase in the shear connectors thickness. The lowest load capacity is observed in the 1 mm thickness model at 218.9 kN, while the highest peak load of 290.7 kN is achieved with the 3 mm thickness. This trend indicates a direct correlation between shear connector thickness and load capacity.

4.2.5. Effect of the Span-to-Depth Ratio

Three spans (3000 mm, 4000 mm, and 6000 mm) with varying depths were analyzed to evaluate the effect of the span-to-depth ratio for the CCFSB with a back-to-back double-channel section with a thickness of 2.3 mm, see Figure 25.

The first peak load generally decreases as the span increases and the span-to-depth ratio increases. For a 3 m span with a ratio of 8, the peak load is 327.3 kN, while for a 4 m span with the same ratio, it rises to 362.4 kN. However, the 6 m span with a ratio of 8 shows a decrease to 320 kN.

For a span-to-depth ratio of 10, the peak loads are lower overall compared to a ratio of 8, with the highest being 355.7 kN for the 6 m span. This suggests that as the span length increases, structural performance may be affected by the ratio, particularly for larger spans.

In contrast, for the span ratios of 16 and 20, the peak loads drop significantly, with the 3 m span at a ratio of 20 yielding only 158.2 kN. This indicates that higher span-to-depth ratios lead to reduced load-carrying capacity, likely due to increased flexibility and reduced stiffness.

4.3. Toughness

Toughness is defined as the ability of a material to absorb energy and deform plastically without fracturing. The area under the load-deflection curve represents the total energy absorbed by the composite cold-formed steel beams (CCFSBs) during the loading process. This area quantitatively reflects the CCFSBs' capacity to withstand deformation and dissipate energy before failure, making it a critical measure for evaluating the structural performance and energy absorption capacity of CCFSBs. The region under the load-deflection curve is the definition of toughness. The results for all the groups are listed in Table 6. Using new geometry, such as sigma, omega, and G sections having the same volumes can increase toughness by different ratios. The double-channel section with ordinary concrete slab serves as the baseline with a toughness of 0%. This allows for a clear comparison with other configurations that either enhance or diminish toughness.

Table 6. Results of the tested parameters.

Beams	First Peak Load (kN)	Deflection at Peak (mm)	Max Deflection (mm)	Toughness (kN·mm)	Percentage of Increase or Decrese in Toughness
DC-OC-110	221.3	33.3	68.1	11,153.5	0
DS-OC-110	251.5	56.5	83.1	17,462	56.6
DG-OC-110	226	33.6	72.8	12,613.8	13.1
DO-OC-110	365.2	75.3	101.6	31,351.8	181.1
DGi-OC-110	380.3	80	100	28,652	156.9
DSi-OC-110	339.5	51.4	100.4	28,812.8	158.3
DC-ECC1-110	224.3	33.7	68.2	11,542.1	3.5
DC-ECC2-110	222.7	32.7	73.4	12,567.7	12.7
DC-ECC3-110	227.5	34.5	77.2	13,600.74	22
DS-ECC3-110	262	46.1	82.9	17,991.5	61.4
DG-ECC3-110	229.3	34.1	73	12,991.14	16.5
DO-ECC3-110	387.4	74.4	102	33,399.8	199.5
DGi-ECC3-110	400.7	77.8	100.1	32,449.6	191
DSi-ECC3-110	384	79.8	101	32,752.2	193.7
DC-OC-70	187.6	31.4	50.3	5938.1	−46.8
DC-OC-90	216.7	34.0	50.6	7707.9	−30.9
DC-OC-110	221.3	33.3	68.1	11,153.5	0
DC-OC-130	229.6	35.7	68.2	11,806.5	5.8
DC-OC-150	258.9	34.6	75.3	15,460.63	38.6
DC-OC-200	332.5	34.03	75.2	20,690.6	85.5
DC-OC-110-L6-2.3	236.6	39.5	71	12,323	10.5
DC-OC-110-L11-2.3	236.7	38.8	73.2	12,981.2	16.4
DC-OC-110-C6-2.3	262.6	52.6	78.8	15,181.8	36.1
DC-OC-110-C11-2.3	260.1	49.8	79	15,600.9	39.9
DC-OC-110-TR6-2.3	260.5	52.3	93.5	19,384.4	73.8
DC-OC-110-TR11-2.3	263.5	53.1	94.7	19,866.6	78.1
DC-OC-110-TR11-1	263.5	53.1	121.1	15,250.5	36.7
DC-OC-110-TR11-2	237.4	50.1	142.1	16,888.0	51.4
DC-OC-110-TR11-3	264.1	52.9	99.8	21,223.7	90.2
DC-OC-110-SH11-1	218.9	33.9	71.1	6237.9	−44
DC-OC-110-SH11-1.5	151.8	32.3	58.7	11,153.5	0
DC-OC-110-SH11-2	247.1	32.9	77.9	15,060.5	35
DC-OC-110-SH11-3	290.7	40.6	77.2	18,247.3	63.6
DC-3-8	327.3	10.1	18.5	4609.8	-
DC-4-8	362.4	16.3	35.8	10,426.6	-
DC-6-8	320	16.7	16.7	3197.3	-
DC-3-10	269.5	10.8	44.1	8609.8	-
DC-4-10	249.0	14.6	36.4	7187.8	-
DC-6-10	355.7	31.5	31.5	7130.7	-
DC-3-16	199.6	23.9	52.2	7818.0	-
DC-4-16	221.3	33.3	68.1	11,153.5	-
DC-6-16	221.7	43.4	44.1	6084	-
DC-3-20	158.2	30.8	104.8	7895.8	-
DC-4-20	153.8	42.2	84	9707.9	-
DC-6-20	190.1	64.1	65.3	7951.6	-

4.3.1. Effect of Different CFS Configurations with Ordinary Concrete and ECC Slabs (110 mm)

The analysis of these results highlights the toughness performance of the different beams with the various beam configurations and with ordinary concrete slabs and ECC slabs, as seen in Figures 26 and 27.

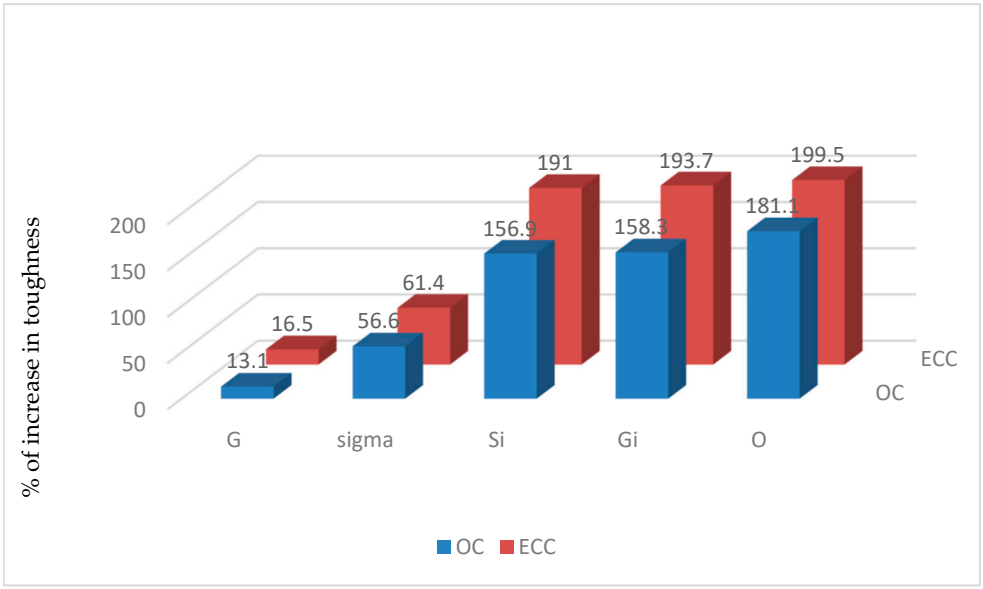

Figure 26. Effect of section geometry and ECC together on the relative toughness (110 mm thickness).

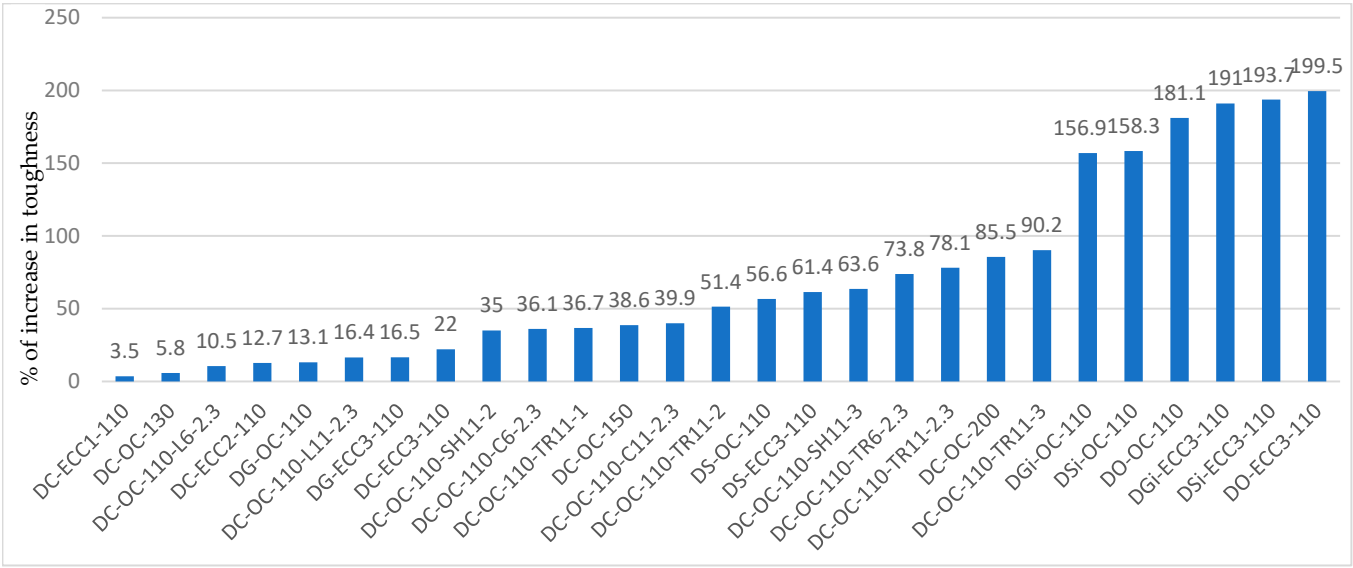

Figure 27. Percentage of increase in toughness for the first group of parametric study.

The double-omega section with ordinary concrete slab exhibits the most substantial increase in toughness at 181.1%. This suggests that the omega design significantly enhances the beam's ability to absorb energy and resist cracking under load. The double-G section with inverted lips and the double-sigma section with inverted lips also show remarkable increases in toughness, with 156.9% and 158.3%, respectively. These results indicate that the inverted-lip feature enhances load distribution and overall resistance to deformation.

The introduction of engineered cementitious composite (ECC) slabs leads to varying increases in toughness. The double-omega section with ECC3 slab achieves an impressive 199.5% increase, highlighting the effectiveness of ECC in enhancing toughness. Other ECC configurations, such as the double-sigma section with ECC3 (61.4%) and the double-G section with ECC3 (16.5%), also show improvements but not as pronounced as the omega section. This underscores the potential of ECC materials in improving structural performance. The findings emphasize the importance of both geometry and material selection in optimizing toughness.

4.3.2. Effect of the Configurations of Proposed Stiffeners

The provided results describe the toughness of double-channel sections with ordinary concrete (OC) slabs, focusing on various stiffener configurations (L, channel, and trapezoidal) and their influence on structural performance, see Figure 27.

Trapezoidal stiffeners show the greatest increase in toughness (73.8%), suggesting they should be prioritized in design for applications requiring high structural integrity. Channel stiffeners provide moderate improvements (39.9%), significantly better than L stiffeners (16.4%) but not as effective as trapezoidal designs.

4.3.3. Effect of the Thickness of Ordinary Concrete Slabs

Six thicknesses—70 mm, 90 mm, 110 mm, 130 mm, 150 mm, and 200 mm—were studied to find the toughness for the double-channel composite cold-formed steel beam with OC slabs, see Figure 27. Thicknesses of 150 mm and 200 mm show an increase in toughness of 38.6% and 85.5%, respectively, which indicates a clear improvement in toughness with the increase in thickness.

4.3.4. Effect of the Span to Depth Ratio

Three spans (3000 mm, 4000 mm, and 6000 mm) with varying depths were analyzed to evaluate the effect of the span-to-depth ratio for CCFSBs with a back-to-back double-channel section with a thickness of 2.3 mm on their toughness, see Figure 28. The toughness values vary significantly with changes in span and span-to-depth ratio. Specifically, the data reveal that both the span and the span-to-depth ratio play critical roles in influencing the structural performance of the double-channel sections.

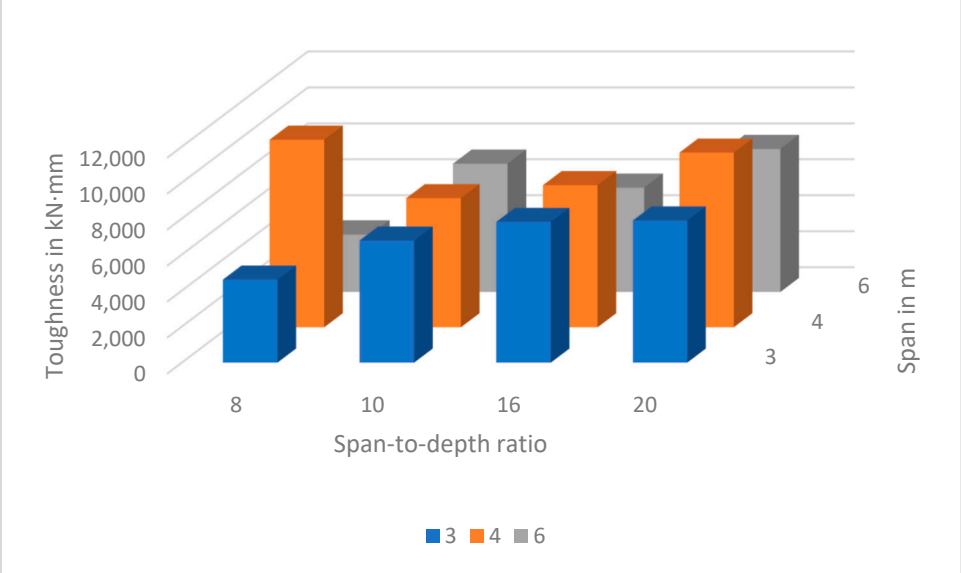

Figure 28. Toughness for the second group of parametric study.

For a 3 m span, toughness values are generally higher across the various span-to-depth ratios, with a peak toughness of 8609.8 kN·mm at a span-to-depth ratio of 10. The 4 m span consistently shows strong toughness values, peaking at 11,153.5 kN·mm for the span-to-depth ratio of 16. The 6 m span exhibits the lowest toughness values overall, with a notable drop to 3197.3 kN·mm at a span-to-depth ratio of 8. This suggests that increasing the span without adequate depth negatively impacts structural performance. The findings suggest that there is an optimal span-to-depth ratio that maximizes toughness, particularly for spans of 4 m. For instance, the highest toughness observed (11,153.5 kN·mm) occurs at this span with a ratio of 16.

5. Conclusions

Numerical investigations were carried out to develop a precious understanding of the full static resistance of CCFSBs. FE models were developed to predict the static resistance of CCFSBs. Based on the results of this study, several conclusions can be drawn.

1. The double-omega section with ordinary and ECC3 slabs exhibits the highest first peak loads (365.2 kN and 387.4 kN) and significant toughness increases (181.1% and 199.5%), demonstrating the omega design's effectiveness in enhancing load capacity and toughness;
2. Inverted-lip sections, like double G and sigma, show high peak loads (380.3 kN and 339.5 kN) and substantial toughness improvements (156.9% and 158.3%), highlighting the benefit of the inverted-lip feature for structural performance;
3. The double-sigma section with ordinary concrete achieves a peak load of 251.5 kN and a toughness increase of 56.6%, indicating its effectiveness among ordinary concrete configurations;
4. Trapezoidal stiffeners significantly improve toughness (73.8% and 78.1% for 650 mm and 325 mm configurations), demonstrating their role in enhancing load distribution and reducing deformation risk;
5. Increasing the thickness of ordinary concrete slabs generally enhances toughness, with the 200 mm thickness achieving an 85.5% increase, underscoring the importance of adequate thickness for structural performance;
6. Toughness values significantly vary with changes in span and span-to-depth ratio.

Author Contributions: Conceptualization, M.T.N.; data curation, O.A.S. and M.T.N.; formal analysis, M.T.N. and O.A.S.; investigation, Y.E.I., O.A.S. and H.M.M.; methodology, M.T.N., I.I. and Y.E.I.; software, O.A.S. and M.T.N.; supervision, M.T.N., H.M.M. and I.I.; validation, O.A.S.; visualization, O.A.S. and M.T.N.; writing—original draft, O.A.S., M.T.N., and Y.E.I.; writing—review and editing, M.T.N. and Y.E.I. All authors have read and agreed to the published version of the manuscript.

Funding: This research received no external funding.

Data Availability Statement: The original contributions presented in the study are included in the article. Further inquiries can be directed to the corresponding author.

Acknowledgments: The authors would like to thank Prince Sultan University for their support and for paying the article processing charges (APC) of this publication.

Conflicts of Interest: The authors declare no conflicts of interest.

References

1. Hsu, C.T.T.; Punurai, S.; Punurai, W.; Majdi, Y. New composite beams having cold-formed steel joists and concrete slab. *Eng. Struct.* **2014**, *71*, 187–200. [CrossRef]
2. Lakkavalli, B.S.; Liu, Y. Experimental study of composite cold-formed steel C-section floor joists. *J. Constr. Steel Res.* **2006**, *62*, 995–1006. [CrossRef]
3. Nguyen, R.P. Thin-Walled, Cold-Formed Steel Composite Beams. *J. Struct. Eng.* **1991**, *117*, 2936–2952. [CrossRef]
4. Wehbe, N.; Bahmani, P.; Wehbe, A. Behavior of Concrete/Cold Formed Steel Composite Beams: Experimental Development of a Novel Structural System. *Int. J. Concr. Struct. Mater.* **2013**, *7*, 51–59. [CrossRef]
5. Irwan, J.M.; Hanizah, A.H.; Azmi, I. Test of shear transfer enhancement in symmetric cold-formed steel–concrete composite beams. *J. Constr. Steel Res.* **2009**, *65*, 2087. [CrossRef]
6. Irwan, J.; Hanizah, A.; Azmi, I.; Koh, H. Large-scale test of symmetric cold-formed steel (CFS)–concrete composite beams with BTTST enhancement. *J. Constr. Steel Res.* **2011**, *67*, 720–726. [CrossRef]
7. Bamaga, S.O.; Tahir, M.M.; Tan, C.S.; Shek, P.N.; Aghlara, R. Push-out tests on three innovative shear connectors for composite cold-formed steel concrete beams. *Constr. Build. Mater.* **2019**, *223*, 288–298. [CrossRef]

8. Bamaga, S.O.; Tahir, M.M.; Ngian, S.P.; Mohamad, S.; Sulaiman, A.; Aghlara, R. Structural behaviour of cold-formed steel of double c-lipped channel sections integrated with concrete slabs as composite beams. *Lat. Am. J. Solids Struct.* **2019**, *16*, e195. [CrossRef]
9. Ma, D.; Rasmussen, K.J.R.; Zhang, H. Test and design of cold-formed steel closed built-up beams with double sigma sections and triple lipped channel sections. *Thin-Walled Struct.* **2023**, *192*, 111192. [CrossRef]
10. Rahnavard, R.; Craveiro, H.D.; Simões, R.A.; Santiago, A.; Laím, L.; Gardner, L. Built-Up Cold-Formed Steel-Lightweight Concrete (CFS-LWC) Composite Beams Subjected to Elevated Temperatures. *Ce/Papers* **2024**, *7*, 202–208. [CrossRef]
11. Rohola, R.; Hélder, C.; Rui, S.; Shahabeddin, T.; Benjamin, S. Understanding the Behavior of Built-Up Cold-Formed Steel Lightweight Concrete (CFS-LWC) Composite Beams. Available online: https://www.researchgate.net/publication/379155554 (accessed on 19 March 2024).
12. Rahnavard, R.; Craveiro, H.D.; Simões, R. Flexural resistance of Cold-formed steel-lightweight concrete (CFS-LWC) composite beam. *Ce/Papers* **2023**, *6*, 176–180. [CrossRef]
13. Ataei, A.; Mahmoudy, S.A.; Zeynalian, M.; Chiniforush, A.A.; Ngo, T.D. Experimental study of innovative bolted shear connectors in demountable cold-formed steel–concrete composite beams. *Thin-Walled Struct.* **2023**, *192*, 111116. [CrossRef]
14. Karimipanah, A.; Zeynalian, M.; Ataei, A. A numerical study on a novel demountable cold-formed steel composite beam with profiled steel sheeting. *Thin-Walled Struct.* **2024**, *199*, 111812. [CrossRef]
15. Ataei, A.; Mahmoudy, S.A. Modeling of innovative bolted shear connectors in demountable cold-formed steel-concrete composite beams: Validation of finite element model and parametric study. *J. Build. Eng.* **2024**, *95*, 110076. [CrossRef]
16. Lee, C.; Bae, B.; Lee, K.; Kim, T. Experimental study on shear performance of composite beam using lipped channels. *Structures* **2024**, *70*, 107707. [CrossRef]
17. Rajić, A.; Lukačević, I.; Skejić, D.; Ungureanu, V. Cold-formed Steel-Concrete Composite Beams with Back-to-Back Channel Sections in Bending. *Civ. Eng. J.* **2023**, *9*, 2345–2369. [CrossRef]
18. Žuvelek, V.; Curkovic, I.; Lukačević, I.; Rajić, A.; Ćurković, I. Numerical Study of the Behavior of the Bolted Shear Connection in Cold-Formed Steel-Concrete Composite beam. Available online: https://www.researchgate.net/publication/364393105 (accessed on 20 October 2022).
19. Majdi, Y.; Hsu, C.T.T.; Zarei, M. Finite element analysis of new composite floors having cold-formed steel and concrete slab. *Eng. Struct.* **2014**, *77*, 65–83. [CrossRef]
20. Alhajri, T.M.; Tahir, M.M.; Azimi, M.; Mirza, J.; Lawan, M.; Alenezi, K.; Ragaee, M. Behavior of pre-cast U-Shaped Composite Beam integrating cold-formed steel with ferro-cement slab. *Thin-Walled Struct.* **2016**, *102*, 18–29. [CrossRef]
21. Mahmoud, N.S.; Abd-rabou, S.E.M.; Ghannam, M.; Abdel-kader, A.A. Experimental and Theoretical Study of Composite Cold Formed SteelConcrete Beams. *Int. J. Sci. Eng. Res.* **2019**, *7*, 1–10.
22. Mahmoud, N.S.; El-Deen, S.; Abd-Rabou, M.; Ghannam, M.; Abdel-Kader, A.A. Proposed Formula for Shear Resistance of Innovative Shear Connector between Cold Formed Steel Section and Concrete. *MEJ-Mansoura Eng. J.* **2020**, *43*, 7–19.
23. Lukačević, I.; Ćurković, I.; Rajić, A.; Čudina, I. Innovative Lightweight Cold-Formed Steel-Concrete Composite Floor System–LWT-FLOOR project. *IOP Conf. Ser. Mater. Sci. Eng.* **2021**, *1203*, 032078. [CrossRef]
24. Ćurković, I.; Lukačević, I.; Žuvelek, V.; Rajić, A. Numerical Investigation of Shear Connection in Cold-formed Steel-concrete Composite Beam. *Ce/Papers* **2022**, *5*, 847–856. [CrossRef]
25. Leal, L.A.A.d.S.; Batista, E.d.M. Composite floor system with cold-formed trussed beams and prefabricated concrete slab Selected and extended contribution of SDSS 2019. *Steel Constr.* **2020**, *13*, 12–21. [CrossRef]
26. Laím, L.; Rodrigues, J.P.C.; Craveiro, H.D. Flexural behaviour of beams made of cold-formed steel sigma-shaped sections at ambient and fire conditions. *Thin-Walled Struct.* **2015**, *87*, 53–65. [CrossRef]
27. Yılmaz, Y.; Öztürk, F.; Demir, S. Buckling behavior of cold-formed steel sigma and lipped channel section beam-columns: Experimental and numerical investigation. *J. Constr. Steel Res.* **2024**, *214*, 108456. [CrossRef]
28. Laím, L.; Rodrigues, J.P.C. Flexural Behaviour of Cold-Formed Steel Beams in Fire Situation. *Rev. Estrut. Aço* **2015**, *4*, 73. [CrossRef]
29. Liu, Q.; Yang, J.; Chan, A.H.C.; Li, L.-Y. Pseudo-plastic moment resistance of continuous beams with cold-formed sigma sections at internal supports: A numerical study. *Thin-Walled Struct.* **2011**, *49*, 1592–1604. [CrossRef]
30. Yang, J.; Luo, K.; Wang, W.; Shi, Y.; Li, H. Research on the flexural buckling behavior of the cold-formed steel back-to-back built-up columns with Σ-section. *Eng. Struct.* **2024**, *302*, 117404. [CrossRef]
31. Anbarasu, M. Simulation of flexural behaviour and design of cold-formed steel closed built-up beams composed of two sigma sections for local buckling. *Eng. Struct.* **2019**, *191*, 549–562. [CrossRef]
32. Szewczak, I.; Rzeszut, K.; Rozylo, P. Structural behaviour of steel cold-formed sigma beams strengthened with bonded steel tapes. *Thin-Walled Struct.* **2021**, *159*, 107295. [CrossRef]
33. Elbacklesh, T.A.; Khalil, N.N.; El-Shenawy, I.M.; Abou-Rayan, A.M. Flexural behavior of cold-formed steel I-beams strengthened in the web with different materials. *J. Constr. Steel Res.* **2024**, *223*, 109083. [CrossRef]

34. *ABAQUS Software*; ABAQUS/CAE 2020: A Computer Software for Finite Element Analysis; Dassault Syst Simulia: Johnston, RI, USA, 2019.
35. *EN 1992-1-1*; Eurocode 2: Design of Concrete Structures-Part 1–1: General Rules and Rules for Buildings. British Standard Institution: London, UK, 2005; Volume 668, pp. 659–668.
36. Le, K.B.; Van Cao, V. Numerical study of circular concrete filled steel tubes subjected to pure torsion. *Buildings* **2021**, *11*, 397. [CrossRef]
37. Beck, J.; Kiyomiya, O. Fundemental Pure Torsional Properties of Concrete Filled Circular Steel Tubes. *Doboku Gakkai Ronbunshu* **2003**, *2003*, 285–296. [CrossRef] [PubMed]
38. Li, G.; Chen, B.; Yang, Z.; Feng, Y. Experimental and numerical behaviour of eccentrically loaded high strength concrete filled high strength square steel tube stub columns. *Thin-Walled Struct.* **2019**, *127*, 483–499. [CrossRef]
39. Winful, D.; Cashell, K.A.; Afshan, S.; Barnes, A.M.; Pargeter, R.J. Behaviour of high strength steel columns under fire conditions. *J. Constr. Steel Res.* **2018**, *150*, 392–404. [CrossRef]
40. Emara, M.; Elsamak, G.; Ghalla, M.; Hu, J.W.; Badawi, M.; Salama, M.I. Shear improvement of defected RC beams with sustainable aluminum boxes incorporating high performance concretes. *Case Stud. Constr. Mater.* **2024**, *21*, e03500. [CrossRef]
41. Carreira, D.J.; Chu, K.-H. Stress-strain relationship for plain concrete in compression. *J. Proc.* **1985**, *82*, 797–804.
42. Jabbar, A.M.; Al-Zuheriy, A.S.J.; Hasan, Q.A. A numerical investigation of the structural behavior of reinforced concrete beams fully or partially encased with UHPC layers in flexure. *Structures* **2024**, *70*, 107706. [CrossRef]
43. Mohammed, T.A.; Abebe, S. Numerical investigation of steel-concrete composite (SCC) beam subjected to combined blast-impact loading. *Heliyon* **2022**, *8*, e10672. [CrossRef]
44. Chen, F.; Yu, Z.; Yu, Y.; Liu, Q. Study on the bond-slip numerical simulation in the analysis of reinforced concrete wall-beam-slab joint under cyclic loading. *Constr. Build. Mater.* **2024**, *449*, 138266. [CrossRef]
45. Hason, M.M.; Al-Janabi, M.A.Q. Behavior of zero cement reinforced concrete slabs under monotonic and impact loads: Experimental and numerical investigations. *Case Stud. Constr. Mater.* **2024**, *21*, e03789. [CrossRef]
46. El-Mandouh, M.A.; Hu, J.W.; Shim, W.S.; Abdelazeem, F.; Elsamak, G. Torsional Improvement of RC Beams Using Various Strengthening Systems. *Buildings* **2022**, *12*, 1776. [CrossRef]
47. Hamoda, A.; Emara, M.; Ahmed, M.; Abadel, A.A.; Patel, V.I. Flexural Behavior of Precast Rectangular Reinforced Concrete Beams with Intermediate Connection Filled with High-Performance Concrete. *Buildings* **2024**, *14*, 2823. [CrossRef]
48. Rahnavard, R.; Razavi, M.; Fanaie, N.; Craveiro, H.D. Evaluation of the composite action of cold-formed steel built-up battened columns composed of two sigma-shaped sections. *Thin-Walled Struct.* **2022**, *183*, 110390. [CrossRef]
49. Zhu, L.; Wang, J.-J.; Li, X.; Tang, L.; Yu, B.-Y. Experimental and Numerical Study of Curved SFRC and ECC composite beams with Various Connectors. *Thin-Walled Struct.* **2020**, *155*, 106938. [CrossRef]
50. Nie, X.; Duan, L.; Zhuang, L.; Ding, R.; Fan, J. Experimental and numerical study on steel-concrete composite frames with engineered cementitious composites. *Eng. Struct.* **2022**, *265*, 114489. [CrossRef]
51. Fan, J.; Gou, S.; Ding, R.; Zhang, J.; Shi, Z. Experimental and analytical research on the flexural behaviour of steel–ECC composite beams under negative bending moments. *Eng. Struct.* **2020**, *210*, 110309. [CrossRef]
52. Lee, C.K.; Khan, M.K.I.; Zhang, Y.X.; Rana, M.M. Engineered cementitious composites (ECC) encased concrete-steel composite stub columns under concentric compression. *Structures* **2020**, *24*, 386–399. [CrossRef]
53. Ji, J.; Zhang, Z.; Lin, M.; Li, L.; Jiang, L.; Ding, Y.; Yu, K. Structural application of engineered cementitious composites (ECC): A state-of-the-art review. *Constr. Build. Mater.* **2023**, *406*, 133289. [CrossRef]
54. Nawar, M.T.; Selim, M.; Zaghlal, M.; El-Zohairy, A.; Emara, M. Performance of GFRP-Confined Rubberized Engineered Cementitious Composite Columns. *J. Compos. Sci.* **2024**, *8*, 330. [CrossRef]
55. Zhou, J.; Pan, J.; Leung, C.K.Y. Mechanical Behavior of Fiber-Reinforced Engineered Cementitious Composites in Uniaxial Compression. *J. Mater. Civ. Eng.* **2015**, *27*, 0001034. [CrossRef]
56. Divya, M.; Kumar, R.S.; George, P.; Jayabalan, P.; Tsavdaridis, K.D.; Bahurudeen, A. Development of novel shear connectors for cold-formed steel concrete composite beams. *Constr. Build. Mater.* **2023**, *387*, 131644. [CrossRef]
57. Yu, W.-W. AISI-Specifications for the Design of Cold-Formed Steel Structural Members. 2016. Available online: https://scholarsmine.mst.edu/ccfss-aisi-spechttps://scholarsmine.mst.edu/ccfss-aisi-spec/197 (accessed on 1 October 2016).